Tailoring the electrical conductivity and domain switching in $BiFeO_3$ ceramics

M. Makarovic[1,2,3,*], N. Kanas[3], A. Zorko[4], K. Ziberna[1], H. Ursic[1,2], D.R. Smabraten[3], S.M. Selbach[3] and T. Rojac[1,2]

[1] *Jozef Stefan Institute, Electronic Ceramics Department, 1000 Ljubljana, Slovenia*

[2] *Jozef Stefan International Postgraduate School, 1000 Ljubljana, Slovenia*

[3] *NTNU Norwegian University of Science and Technology, Department of Materials Science and Engineering, 7491 Trondheim, Norway*

[4] *Jozef Stefan Institute, Department of Condensed Matter Physics, 1000 Ljubljana, Slovenia*

*Corresponding author: maja.makarovic@ijs.si (Maja Makarovič)

+386 1 477 3260

Electronic Ceramics Department

Jozef Stefan Institute

Jamova cesta, 39, Ljubljana

Slovenia, SI-1000

Abstract

In this report, the influence of cobalt doping and annealing atmosphere on the electrical conductivity and polarization switching of BFO ceramics was studied. Electrical conductivity as well as hardening behavior has been found to increase with introduction of acceptor Co'_{Fe} sites. BFO ceramics doped with Co exhibit p-type conductivity, dominated by Fe^{4+} defects, which can be successfully reduced during high-temperature annealing in N_2. However, indications of local reduction were found, presumably on domain walls and grain boundaries. A mechanism of hardening is proposed, which assumes two types of pinning centers related to defect complexes of: i) V_{Bi}''' and $Fe^{\bullet}_{Fe}$ and ii) Co'_{Fe} and $V_O^{\bullet\bullet}$. Such pinning centers are shown to play a key role in the hardening behavior and hysteresis loop pinching and biasing. The results of this study could further promote design of local and bulk conductivity as well as hardening properties of BFO-based materials.

Key words: ceramics, ferroelectric, point defects, conductivity, hardening

1 Introduction

Ferroelectric ceramic materials are widely used in piezoelectric devices, such as sensors, actuators, transducers and memory devices. The macroscopic piezoelectric response of these materials is strongly affected by the displacements of domain walls (DWs) under applied external electric or stress fields [1,2], which are strongly influenced by the dynamic interactions of DWs with charged point defects [3–6]. In $Pb(Zr,Ti)O_3$ (PZT), the market-dominating piezoelectric material, these interactions may be tuned by acceptor or donor doping, resulting, respectively, in the so-called hardening and softening effects, which are the most important concepts for tailoring functional properties of this group of materials for specific applications [7].

Due to the toxicity and low operating temperatures (<~250 °C) of PZT, intensive research has been devoted to to develop PZT alternatives [8,9]. Bismuth ferrite, $BiFeO_3$ (BFO), is a promising lead-free candidate for high-temperature piezoelectric applications due to its extremely high Curie temperature of ~825 °C [10]. However, practical applications of BFO have been restricted by the high electrical conductivity, which is commonly attributed to the varying valence states of Fe ion (2+, 3+, 4+) and the corresponding compensating defects [11–19].

The macroscopic hardening behavior of BFO, reflected in pinching/biasing of the ferroelectric hysteresis loop and aging [20,21], appears similar to that of acceptor doped ("hard") PZT [7]. In "hard" PZT this behavior has been attributed to the presence of oxygen vacancies ($V_O^{\bullet\bullet}$), bound to acceptor centers in acceptor-oxygen-vacancy defect complexes [3,22,23]. Similarly, hardening in BFO and, in particular, the associated elevated electrical conductivity, have been attributed to the effect of acceptor-oxygen-vacancy defect complexes, such as $Fe'_{Fe} - V_O^{\bullet\bullet}$ (where Fe'_{Fe} indicates Fe^{2+} on Fe^{3+} lattice site) or $V_{Bi}''' - V_O^{\bullet\bullet}$ (where V_{Bi}''' is bismuth vacancy) [24–29].

A number of independent experimental and theoretical studies on BFO and related materials, suggest p-type conductivity when BFO is sintered in air [15,16,30–36]. A recent study on BFO-related ceramics demonstrated a transition from n- to p-type conduction on increasing $p(O_2)$ from ~10^{-6} to 1 atm in the temperature range 650-800 °C [19]. The proposed defect model for such behavior assumes two defect reactions related to: i) volatilization of Bi_2O_3 at elevated

temperatures (equation (1.1), resulting in formation of V_{Bi}''' and $V_O^{\bullet\bullet}$, and ii) reduction/oxidation of Fe^{3+} (equation (1.2) and (1.3)), respectively), which is determined by the partial pressure of O_2 during annealing and results either in the formation of reduced Fe^{2+} (Fe'_{Fe}) or oxidized Fe^{4+} ($Fe^{\bullet}_{Fe}$) states.

$$2Bi^x_{Bi} + 3O^x_O \leftrightarrow 2V'''_{Bi} + 3V^{\bullet\bullet}_O + 2Bi(g) + \frac{3}{2}O_2(g) \tag{1.1}$$

$$2Fe^x_{Fe} + O^x_O \leftrightarrow 2Fe'_{Fe} + V^{\bullet\bullet}_O + \frac{1}{2}O_2(g) \tag{1.2}$$

$$2Fe^x_{Fe} + V^{\bullet\bullet}_O + \frac{1}{2}O_2(g) \leftrightarrow 2Fe^{\bullet}_{Fe} + O^x_O \tag{1.3}$$

Rojac *et al.* provided atomic-scale chemical and structural evidence on segregation of V_{Bi}''' and $Fe^{\bullet}_{Fe}$ at conductive DWs in BFO ceramics [37], explaining the p-type DW conduction [17]. On the other hand, studies on thin films indicate n-type conductive DWs [38], which is probably related to different processing conditions in terms of temperature and $p(O_2)$. None of these provide a clear picture of how these accumulated defects could be used to control DW mobility and macroscopic electrical and electromechanical properties.

Literature reports therefore clearly suggest a complex interplay between different types of defects ($V_O^{\bullet\bullet}$, Fe^{2+}, Fe^{4+}), their location (DWs) and association (defect complexes), which makes the microscopic origin(s) of hardening in BFO still unclear. In particular, control over the hardening behavior in BFO, which is a very important for applications, has not yet been achieved. In this study, we introduced points defects in BFO ceramics and investigated how these defects affect the electrical conductivity and domain wall pinning. To achieve this, we used a combined approach of acceptor doping BFO with Co (introduction of acceptor Co'_{Fe} sites) along with post-annealing in different oxygen partial pressures, allowing us to finely control the compensating defects and the extent of redox reactions, respectively.

We found that the electrical conductivity and pinching/biasing of *P-E* loop in Co-doped BFO ceramics increases as the concentration of dopant increases. In addition, we found that Co-

doped BFO ceramics exhibit p-type conductivity, dominated by Fe^{4+} defects, which can be successfully reduced during high-temperature annealing in nitrogen. A combination of results obtained by *in-situ* AC and DC conductivity measurements, Seebeck coefficient measurements and conductive-atomic force microscopy (c-AFM) indicates that this reduction most probably occurs locally, presumably on domain walls and grain boundaries. Considering the literature and the overall data on polarization switching, conductivity behavior and defect analysis using EPR, a mechanism of hardening is proposed. We assume there are two types of pinning centers related to: i) V_{Bi}''' and $Fe_{Fe}^{\bullet}$ related, which tend to accumulate at DWs and ii) Co_{Fe}' and $V_O^{\bullet\bullet}$ related, most probably bound into complexes, which are shown to play the key role in the hardening behavior and hysteresis loop pinching and biasing. These results imply that the local and bulk conductivity as well as hardening properties of BFO-based materials can be tailored through dopants and thermoatmospheric history.

2 Experimental

The $Bi(Fe_{1-x}Co_x)O_3$ ceramics with x = 0.0025, 0.005, 0.1 and 0.015, subsequently referred as 0.25 Co, 0.5 Co, 1 Co and 1.5 Co, were prepared by conventional solid state synthesis. The starting powders Bi_2O_3 (Alfa Aesar, 99.999%), Fe_2O_3 (Alfa Aesar, 99.998%) and Co_3O_4 (Alfa Aesar, 99.0%) were milled separately and homogenized into mixtures of stoichiometric ratio. The powder mixtures were calcined onto a Pt foil substrate at 740 °C for 4 h with a heating and cooling rate of 10 °C min^{-1}. The calcination step was followed by milling in a planetary mill. All powders and powder mixtures in this study were planetary milled at the same conditions, i.e., at 200 min^{-1} of main-disc rotational frequency for 4 h in absolute ethanol using a Retsch PM400 mill (Haan, Germany). All milling steps were performed in polyethylene vials with yttria-stabilized-zirconia (YSZ) milling balls (Ø = 3 mm). Finally, the calcined powders were pressed into pellets/bars by uniaxial (50 MPa) and cold isostatic pressing (300 MPa) and sintered at 800 °C for 4 h with a heating/cooling rate of 10 °C min^{-1}.

The influence of annealing atmosphere was investigated on sintered pellets that were post-annealed i) at 700 °C with zero holding time and with a heating/cooling rate of 2 °C min^{-1} in flowing N_2 (Messer, 4.6), or ii) at 700 °C with 24 h hold time and heating rate of 5 °C and cooling rate of 0.5 °C min^{-1} in 10 atm O_2. As-sintered samples were used as a reference.

Powders samples for X-ray diffraction (XRD) measurements were prepared by crushing the sintered pellets and the phase composition was determined using an X'Pert PRO MPD diffractometer with Cu-Kα1 radiation (PANalytical, Almelo, Netherlands) and the X'Celerator

detector. The XRD patterns were collected in the 2θ range from 10° to 78° using a step of 0.016° and an integration time of 100 s. The data were analyzed with the X'Pert High Score software package using crystallographic cards from the PDF-2 database. The amount of secondary phase $Bi_{25}FeO_{40}$ was determined by Rietveld refinement method using TOPAS software package [39].

Samples for electrical measurements were cut from the sintered pellets and grinded down to a thickness between 0.2 and 0.3 mm. The samples were sputtered with Au electrodes using a circular mask with a diameter of 5 mm (5pascal SRL, Trezzano, Italy).

The dielectric measurements in the frequency range 10^5-10^2 Hz were performed using a 4284A precision LCR meter (Hewlett Packard, Tokyo, Japan), while the measurements in the low frequency range 10^3-10^{-2} Hz were performed with a charge amplifier (Type 5018, Kistler, Winterthur, Switzerland) coupled with a lock-in amplifier (model SR830 DSP, Stanford Research System, Sunnyvale, California). The field amplitude was 0.02 kV cm^{-1}.

Current-density-electric-field (*j-E*) response was measured using a Keithley 237 (Keithley Instruments, Ohio, USA) high voltage source measure unit. The samples were exposed to step-like voltages within the range of ±0.02 kV cm^{-1}. In this range, from negative to positive polarity, 11 field steps were applied. Upon each step, the voltage was maintained constant for 1 h for the current to stabilize, before being recorded (the time-stabilized current is represented as the leakage current). The specific DC electrical conductivity (σ_{DC}) was determined from the *j-E* curves as the curve slope.

The polarization versus electric field (*P-E*) hysteresis loops were measured using an Aixacct TF 2000 analyzer (aixaCCT Systems Gmbh, Aachen, Germany). The samples were immersed in silicone oil and the hysteresis loops were recorded by applying sinusoidal waveforms of 100 Hz at selected electric field amplitudes. The coercive field (E_c) was determined as $E_c = (|E_c^+| + |E_c^-|)/2$. The internal bias field (E_{ib}) indicating a shift of the polarization loop along the abscissa was calculated as $E_{ib} = (E_c^+ + E_c^-)/2$ [40].

Electrical conductivity as a function of temperature in different flowing gases (N_2, O_2) was measured using a direct current (DC) four-point method, as previously reported by Wærnhus *et al*. [41]. Sintered bars were ground down and polished to dimensions of about $15 \times 4 \times 4$ mm. A constant voltage of 1.5 V was applied (GW Instek GPS3030DD) over the sample. The voltage drop and current across the sample was measured using Keithley 2000 multimeters with the electrodes placed 5 mm apart. The temperature was controlled by an S-type thermocouple. The

DC electrical conductivity measurements were performed during annealing of the samples in three consecutive cycles. The samples were annealed from RT to 700 °C with zero holding time and with a heating/cooling rate of 2 °C min^{-1} first in flow of O_2 (Linde, 5.0), afterwards in N_2 (Linde, 5.0) and finally again in O_2.

The Seebeck coefficient (*S*) was measured on ceramic bars analogous to those used for DC conductivity measurements. The measurements were provided using a ProboStat^{TM} setup (NorECs AS), covered by an alumina tube. The setup was placed inside a vertical tubular furnace, where the middle thermocouple was connected to the temperature controller. The top and bottom thermocouple and electrodes were connected to a computer through a multimeter (Keithley 2000). The temperature gradient was measured by two S-type thermocouples. The Seebeck coefficient measurements were performed during annealing of the samples in three consecutive cycles. The samples were annealed from RT to 700 °C with zero holding time and with a heating/cooling rate of 2 °C min^{-1} first in flow of synthetic air (Linde, 5.0), afterwards in N_2 (Linde, 5.0) and finally again in synthetic air.

Dielectric properties as a function of temperature and in different flowing gases (synthetic air, N_2) were investigated using a frequency analyzer (Alpha-A High Performance Frequency Analyser, Novocontrol Technologies, Germany), connected to a ProboStatTM setup in a vertical tubular furnace. The surface of sintered pellets was ground down to ~3 mm, covered with a gold paste for the electrode and annealed to 750 °C with 1 h holding time in order to consolidate the electrode. The measurements were performed at the frequency of 1 Hz during continuous heating/cooling in synthetic air and N_2, the same as in the case of DC electrical conductivity measurements and Seebeck coefficient measurements.

The X-band (9.5 GHz) electron paramagnetic resonance (EPR) measurements were performed on a Bruker EMX spectrometer. The EPR spectra were recorded in the temperature range from RT to 400 °C. Powders for analysis were prepared by crushing the sintered pellets. The g values were obtained from the relationship $h\nu = g\mu_B H$, where ν is operating frequency, μ_B is Bohr magneton and h is Planck's constant.

Samples for conductive atomic force microscopy (c-AFM) analyses were ground with SiC papers, polished with a diamond paste and, finally, chemically etched by polishing for 2 h using a suspension consisting of 60 ml of OP-S colloidal suspension (Struers), 0.3 g of dissolved potassium hydroxide and 440 ml of deionized water. The final thicknesses of the as-prepared samples were ~150 μm. The c-AFM images were recorded using an atomic force microscope

(AFM, Asylum Research, Molecular Force Probe 3D, Santa Barbara, CA, USA) equipped with an ORCA mode. A tetrahedral Si tip on a Si cantilever, both coated with Ti/Ir (Asyelec, AtomicForce F/E GmbH), was used. The c-AFM experiments were conducted by applying a DC voltage between the tip and a bottom electrode. A range of DC voltages (from x to y) was used for c-AFM imaging. Ceramic samples used for conductive atomic force microscopy (c-AFM) analyses were post-annealed (after the sintering) in air at 840 °C with zero holding time and a heating/cooling rate of 10 °C.

3 Results and discussion

3.1 The influence of cobalt concentration on domain switching and electrical conductivity in Co-doped BFO ceramics

Polarization-electric field (*P-E*) loops of BFO ceramics with 0.25, 0.5, 1 and 1.5 at% of Co are shown in Figure 1a. The displayed loops were obtained at electric field amplitude of 100 kV cm^{-1}. All the loops exhibit a pinched and biased shape, typical for BFO ceramics [21,24,42]. This behavior has been previously discussed in terms of DW pinning effect mediated by charged point defects [20,43]. It can be observed that the pinching of *P-E* loop increases as the content of Co increases (indicated with arrow in Figure 1a). Moreover, the applied electric field of 100 kV cm^{-1} is insufficient for switching the domains in 1 and 1.5 at% Co doped sample, evidenced by the underdeveloped *P-E* loops. The *P-E* loops of these two samples eventually develop the shape characteristic for domain switching by applying a higher electric field of 130 kV cm^{-1} (Figure 1b). Also in this case, it is clear that the pinching is increasing with Co concentration. Note that a comparable concentration of secondary phases found in these samples (see Supplementary material, Fig. S1) allows to clearly evaluate the effect of the dopant.

Current-electric field (*I-E*) loops of all Co doped compositions are shown in Figure 1c. Note that the loops were measured at different electric field amplitudes, i.e., 100 kV cm^{-1} (0.25 Co), 110 kV cm^{-1} (0.5 Co), 130 kV cm^{-1} (1 Co) and 150 kV cm^{-1} (1.5 Co) due to different coercive and breakdown fields for the different compositions. Considering these conditions, the coercive field (E_c), internal bias (E_{ib}) and reverse electric field (E_{rev}) as a function of Co concentration were determined and the results are presented in Figure 1d. E_{ib} represents the shift of the loop in the electric-field axis, typically interpreted in terms of the preferential orientation of defects responsible for the DW pinning behavior, which is set by the applied electric field during P-E measurements [44]. Similarly, E_{rev} corresponds to the field of the electric-current peak observed

after the main switching event when reversing the field polarity from positive to negative (see arrow in Figure 1c). This current peak and the associated E_{rev} reflect the back-switching of domains, provoked by the defect-mediated pinning, meaning that the higher E_{rev} (i.e., the more the peak is closer to zero field), the stronger the back-switching, and thus the pinning effects. As it can be observed in Figure 1d, all the three parameters, i.e., E_c, E_{ib} and E_{rev}, clearly increase with increasing Co concentration. These results suggest an increasing hardening effect with increasing acceptor dopant concentration, similar to that observed in acceptor-doped PZT [44].

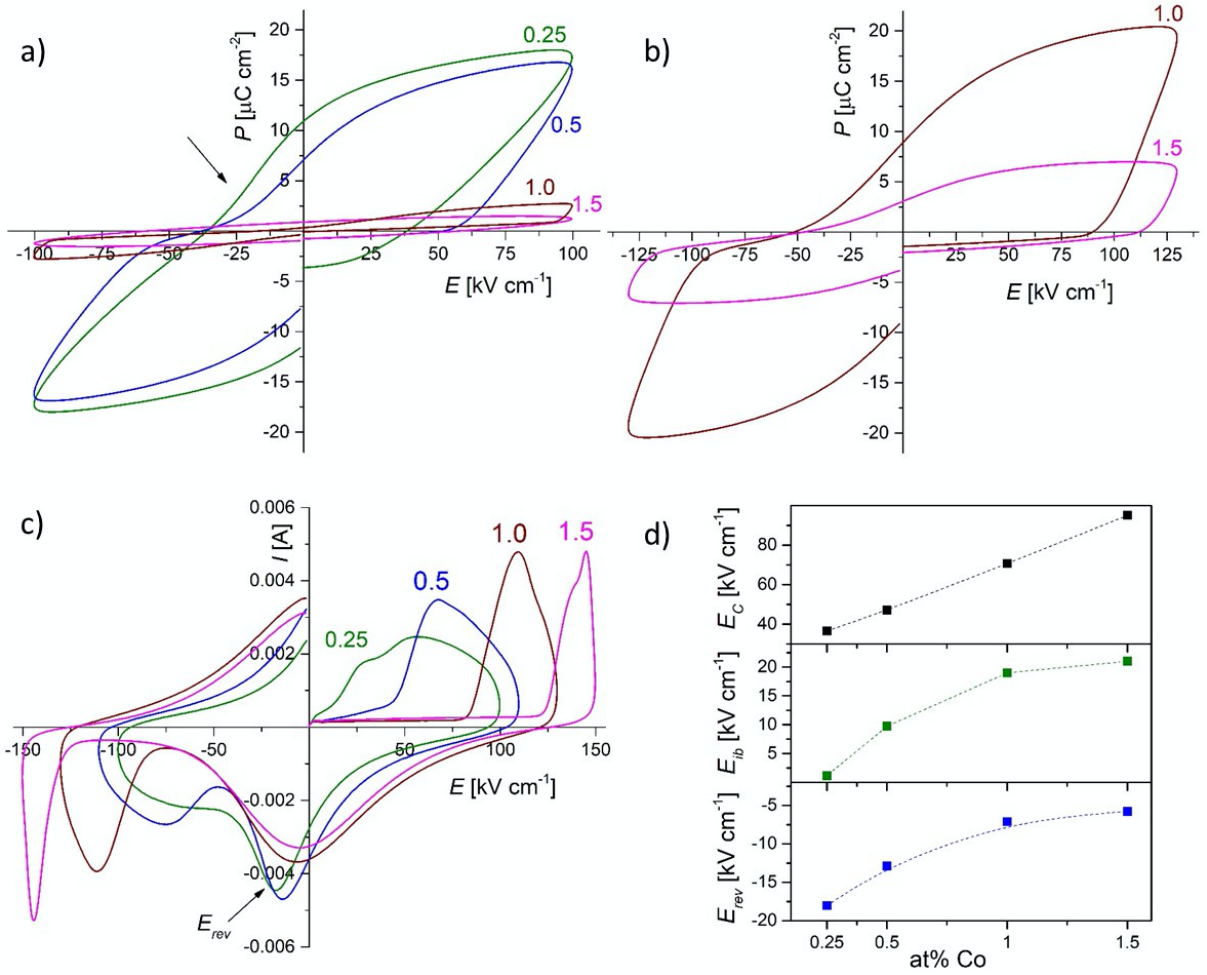

Figure 1: P-E hysteresis loops of BFO ceramics with a) 0.25, 0.5, 1 and 1.5 at% of Co measured at 100 kV cm^{-1} and with b) 1 and 1.5 at% Co measured at 130 kV cm^{-1}. c) I-E loops of Co-doped BFO ceramics; the arrow indicates electric field which corresponds to E_{rev}. d) Compositional dependence of E_C, E_{ib} and E_{rev} (see text for explanations).

Figure 2 shows the real (ε') and imaginary (ε'') part of the dielectric permittivity and the real part of electrical conductivity (σ') as a function of frequency (ω) for the different Co-doped samples. The significant increase in ε'' at low frequencies (<1 Hz) in all samples (Figure 2b; note the logarithmic scale) implies that the dielectric response at low frequencies is dominated by the electrical conduction. However, the dispersion of both ε' and ε'' at low frequencies

indicates that the conduction process not only dissipate energy but also contribute to dielectric polarization of the material, which could be attributed to Maxwell-Wagner-like (M-W) and/or hopping conductivity mechanism [45,23,18]. In addition, except for 0.25 Co, all samples show small relaxation-like features in the ε' curves. As it can be observed from the frequency dependence of σ' in Figure 2c, all four compositions, except for the 0.25% Co doped sample, exhibit a clear pleateau at low frequencies (see dashed lines in Figure 2c). From the frequency dependent σ', it is possible to estimate the specific electrical DC conductivity (σ_{DC}) using the equation [45]:

$$\sigma' = \sigma_{DC} + \omega\varepsilon_0\varepsilon_d'' \tag{3.1}$$

where ε_d'' is the imaginary dielectric permittivity related to polarization losses and ε_0 is the permittivity of vacuum. Providing ε_d'' is low, the equation shows that at low frequencies, the term $\omega\varepsilon_0\varepsilon_d''$ becomes exceedingly small and the σ' eventually reaches a plateau at the low frequency limit corresponding to σ_{DC}, which can be thus estimated as $\sigma' \sim \sigma_{DC}$. Thus, the DC conductivity clearly increases with increasing concentration of Co. The σ' of the 0.25% Co still shows frequency dependence and would probably level off only at lower frequencies than those used for the measurements. Assuming this, we can estimate the σ_{DC} as $< \sim 5 \times 10^{-11}$ $\Omega^{-1}m^{-1}$ for this composition. By extrapolating the plateau of σ' (or onset of the plateau in the case of 0.25% Co) at low frequencies, it can be inferred that the value of σ_{DC} spans from $\sim 5 \times 10^{-11}$ (0.25 Co) to $\sim 4.8 \times 10^{-7}$ $\Omega^{-1}m^{-1}$ (1.5 Co), thus showing an almost 4 orders of magnitude difference within the entire doping range. These σ_{DC} values are in a reasonable agreement with those determined from static current-density-electric-field (*j-E*) measurements (see σ_{DC} values in Figure 2d and inset), confirming the increasing trend of σ_{DC} with increasing Co concentration.

Several experimental and theoretical studies in the literature demonstrate that unmodified BFO-based ceramics exhibit p-type (Fe^{4+}) conductivity when sintered in air [15,14,17,16,30,19]. In line with the defect chemistry model [19], the increase of electrical conductivity in the range 0.25-1.5 at% Co (see Figure 2) could be explained with an increase in the concentration of electron holes (Fe^{4+}). Therefore, these results indicate that Co acts as acceptor dopant according to the defect reaction in equation (3.2) where the Co^{2+} acceptor substituting on the Fe^{3+} site in BFO is proposed to be charge compensated by oxygen vacancies ($V_O^{\bullet\bullet}$):

$$2CoO \xrightarrow{Fe_2O_3} 2Co'_{Fe} + 2O_O^x + V_O^{\bullet\bullet} \quad (3.2)$$

Considering that the concentration of $V_O^{\bullet\bullet}$ is closely related to the valence state of Fe through equation (1.3), increasing the $V_O^{\bullet\bullet}$ concentration by Co doping will shift equation (1.3) towards the right, resulting in more Fe^{4+} and thus favour and enhance p-type conductivity. This assumption is in agreement with synchrotron X-ray absorption spectroscopy (XAS) study on Co-doped BFO ceramics, which confirmed the presence of Fe^{4+} states induced by Co doping [46]. Moreover, this is also in agreement with recent photoelectron spectroscopy study on Co-doped BFO thin films, which revealed that Co is mostly in the oxidation state of 2+ [47].

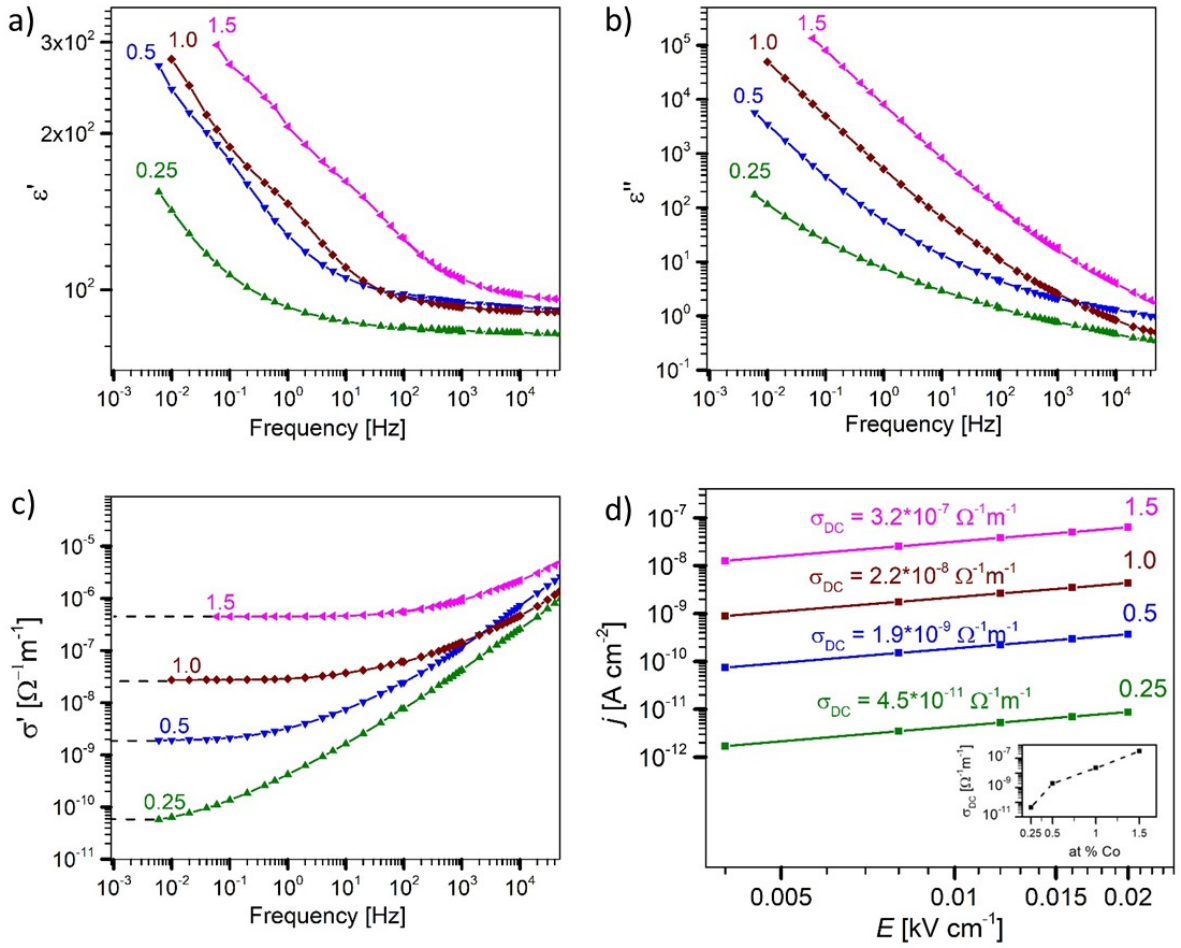

Figure 2: a) Real (ε′) and b) imaginary (ε′′) component of the dielectric permittivity and c) the real part of electrical conductivity (σ′) as a function of driving-field frequency for Co-doped BFO ceramics. In panel d) j-E curves for positive electric fields are displayed for Co-doped BFO ceramics. Note that the j-E measurements were performed by applying both positive and negative field polarity, though, for clarity, the data are shown only for positive electric fields. The inset shows log-linear plot of σ_{DC} as a function of Co concentration. The dashed line between the experimental points is drawn as a guide to the eyes.

Using a similar reasoning as for the electrical conductivity trend with respect to the dopant concentration, the increase of the hysteresis pinching and biasing with increasing Co

concentration (see Figure 1) could be attributed to the increased concentration of defects, i.e., $V_O^{\bullet\bullet}$ and $Fe_{Fe}^{\bullet}$. Both types of defects can, in fact, act as pinning centers for the domain walls, restricting their motion and thus resulting in impeded polarization switching as indicated in Figure 1.

3.2 The influence of annealing atmosphere on domain switching and electrical conductivity in Co-doped BFO ceramics

In order to further elucidate whether and which of those defects dominate the domain-wall pinning behavior, in the next step we control the concentration of $V_O^{\bullet\bullet}$ and $Fe_{Fe}^{\bullet}$ (see equation (1.3)) by thermal treatment of samples in atmospheres with different p(O_2). Considering that the effect of pinching and conductivity is most pronounced in 1.5 at% Co doped BFO ceramics, we further focus on this composition. To investigate the influence of the different type and concentration of defects on electrical conductivity and domain switching, annealing of sintered samples in 10 atm O_2 and N_2 was adopted. In Figure 3a, the *P-E* hysteresis loops of 1.5 at% Co doped BFO ceramics after annealing in 10 atm O_2 and N_2 are displayed along with the *P-E* loop of the as-sintered sample as a reference. It can be observed that after annealing in 10 atm O_2, the loop is still pinched but opens up, suggesting facilitated polarization switching. On the contrary, after annealing in N_2, switching is remarkably reduced as seen by the underdeveloped hysteresis in Figure 3a (see also inset of Figure 3a showing the *P-E* loop after N_2 annealing measured at 160 kV cm^{-1}). Similarly, relative to the sample annealed in air with E_c =80 kV cm^{-1}, the E_c is reduced after annealing in O_2 (E_c =70 kV cm^{-1}), while strongly increased after annealing in N_2 (E_c = 120 kV cm^{-1}).

We propose that the significant domain switching behavior (Figure 3) and thus DW pinning effects by N_2/O_2 annealing are dominated by the different concentration of $V_O^{\bullet\bullet}$, which are known to act as strong pinning centers for DWs in, e.g., undoped and acceptor-doped PZT [3,4]. Therefore, the facilitated domain switching after annealing in O_2 could be related to a decreased concentration of $V_O^{\bullet\bullet}$ pinning centers due to oxidation (see equation (1.3) shifted to the right) and, potentially, a reduction of the Co_{Fe}' pinning centers (due to Co^{2+}-to-Co^{3+} oxidation as shown in equation (3.3)).

$$2Co_{Fe}' + V_O^{\bullet\bullet} + \frac{1}{2}O_2(g) \leftrightarrow 2Co_{Fe}^{x} + O_O^{x} \tag{3.3}$$

Inversely, the reduced polarization switching due to pinning effects observed after annealing in N_2 could be explained with increased concentration of $V_O^{\bullet\bullet}$ (equation (1.3) shifted to the left).

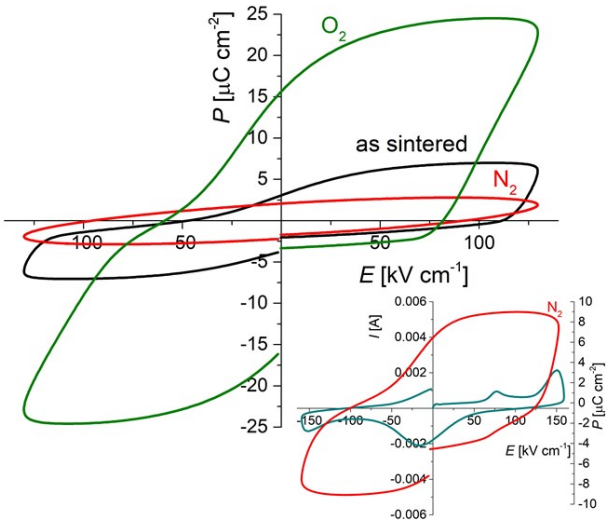

Figure 3: P-E loops of as-sintered 1.5 at% Co doped BFO ceramics, annealed in 10 atm O_2 and N_2 at 130 kV cm^{-1}. The inset displays P-E and corresponding I-E loop of N_2-annealed sample at 160 kV cm^{-1}.

In Figure 4, ε', ε'' and σ' as a function of frequency for 1.5 at% Co-doped ceramics annealed in 10 atm O_2 and N_2 are shown together with the as-sintered sample as a reference. As it can be observed, there are only small differences between the permittivity of as-sintered and 10-atm-O_2-annealed sample. However, the sample annealed in N_2 exhibits a strong step-like increase in ε' at low frequencies, accompanied with a peak in ε'' and a step in σ', clearly suggesting a relaxation process that is induced by annealing in N_2. We suggest here that this relaxation is of a M-W origin, as discussed for BFO-related materials [33,48], arising due to local differences in the electrical conductivity of the sample. These conductivity differences might stem from the localized (inhomogeneous) reduction in N_2 and thus uneven distribution of major charge carriers (Fe^{4+}), similarly as previously suggested for KBT-modified BFO [33]. In the simplest scenario, assuming an equivalent circuit model consisting of a low conductive thin layer connected in series with a conductive bulk [33,49], the lower plateau in σ' step at low frequencies (<10^{-2} Hz) in Figure 4c should correspond to the low-conductive (reduced) region(s). Following this reasoning, from the plateau (dashed line) in σ' (see equation (3.1)), it was estimated that the N_2 annealing lowered the σ_{DC} by an order of magnitude, i.e., from $\sim 5 \times 10^{-7}$ (as-sintered) to $\sim 1 \times 10^{-8}$ $\Omega^{-1}m^{-1}$ (N_2). We finally note that the local nature of the reduction in N_2 is consistent with the fast kinetics of the redox reactions as determined using isothermal DC conductivity measurements in switching atmospheres (see Supplementary material, Fig. S2).

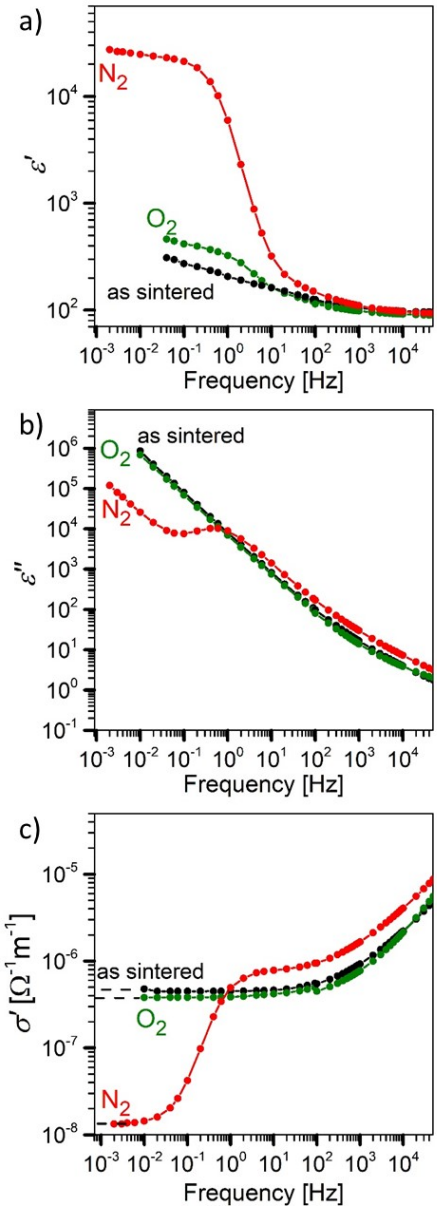

Figure 4: a) ε′, b) ε″ and c) σ′ as a function of driving-field frequency for 1.5 at% Co doped BFO ceramics annealed in 10 atm O_2 and N_2 together with as-sintered sample for reference.

In contrast to the reduced conductivity in N_2, which is well consistent with the literature data [17,19,50,35,51], the negligible change in the conductivity after annealing in 10 atm O_2, with respect to air annealing, i.e., as-sintered sample, (see Figure 4c), is more difficult to explain. Although further analyses would be needed, a possible explanation is that Co^{2+} would be preferably oxidized to Co^{3+} state, rather than Fe^{3+} to Fe^{4+} [47], leading to little changes in the Fe^{4+} concentration and thus conductivity.

3.3 The influence of annealing atmosphere on type and concentration of mobile charged defects in Co-doped BFO ceramics

The explanation of DW pinning effects and the associated loop pinching behavior in the previous section assumes that in the analyzed p(O_2) range, i.e., from ~10^{-6} to 10 atm, the conductivity is still p-type. In order to confirm this, *in-situ* measurements of AC conductivity and Seebeck coefficient as a function of temperature and annealing atmosphere, i.e., in synthetic air/O_2 and N_2, are analyzed next. The results are presented in Figure 5 where the curves labeled 1, 2 and 3 refer to cooling cycle in air/O_2, heating cycle in N_2 and cooling cycle in N_2, respectively. In case of annealing in air, only the curve obtained during cooling cycle is shown (1) as no observable changes between the heating and cooling cycle were observed.

In Figure 5a, it can be seen that the conductivity, represented by σ' measured at 1 Hz, increases with increasing temperature, as expected. It can be observed that upon heating in N_2 (2), the curve traces that measured in air during cooling (1) but only up to ~550°C when the conductivity in N_2 reaches a plateau and deviates from the trend measured in air (compare curves 1 and 2 above 550°C). Upon cooling in N_2 (curve 3), the conductivity decreases as expected, however, the absolute conductivity value is lower than that measured during heating in N_2 (curve 2), all the way down to 150°C, suggesting a decrease in the conductivity of the sample after annealing in N_2. Qualitatively, the same behavior was reported for KBT-modified BFO, in agreement with the p-type conductivity of BFO and related materials [17,19,33,50]. According to the proposed defect model of BFO [19], annealing in N_2 leads to reduction of Fe^{4+} into Fe^{3+}, creating positively charged $V_O^{\bullet\bullet}$, according to the left-shifted equation (1.3). By further inspecting the real part of dielectric permittivity presented in Figure 5b, it can be observed that during cooling in N_2 (curve 3), a strong step-like feature appears in ε', accompanied by a peak in $\tan\delta$ (indicated by green arrow in Figure 5c, curve 3). It is assumed that this anomaly is not related to a phase transition as there is no expected structural transformation in this temperature range [10]. We thus suggest that the anomaly is related to a M-W-like relaxation induced by N_2 annealing, which is consistent with relaxation measured in the permittivity at room temperature after annealing in N_2 (see Figure 4).

Importantly, the differences observed in the AC conductivity measurements after annealing in N_2 were fully recovered after re-annealing the sample in air (see Supplementary material, Fig. S3a), demonstrating that this process is reversible and that the observed changes are not related to secondary phenomena such as e.g., formation of secondary phases.

The Seebeck coefficients of 1.5 at% Co doped BFO ceramics obtained during cooling cycle in O_2 (curve 1), heating cycle in N_2 (curve 2) and cooling cycle in N_2 (curve 3) are presented in Figure 5d. First, the Seebeck coefficient is positive in the whole temperature range by annealing both in air and N_2, confirming that the sample maintains a dominating p-type conductive behavior where Fe^{4+} are the major charge carriers. However, in N_2 the magnitude of Seebeck coefficient significantly increases at lower temperatures during cooling (curve 3 in Figure 5d). This effect is reproducible and reversible by post annealing the N_2-annealed samples back in O_2 (see Supplementary material, Fig. S3b). We propose that the large increase in *S* is intimately related to the relaxation in the dielectric permittivity induced by N_2 annealing (see Figure 4 and Figure 5), arising due to inhomogeneous reduction in N_2 and creation of regions inside the ceramics with variable electrical conductivity. Considering the general relationship between the Seebeck coefficient (*S*) and charge carrier concentration (*C*) expressed as [52]

$$S \propto ln\frac{1-C}{C} \tag{3.4}$$

we can infer that regions of reduced p-type carrier concentration inside BFO upon reduction in N_2 should exhibit higher Seebeck coefficient. Indeed, simple modeling of Seebeck effects in composites showed that introducing a component with lower conductivity in series can considerably increase the total Seebeck coefficient of the composite [53]. We therefore suggest that the increase of Seebeck coefficient in the low temperature range upon cooling in N_2 (Figure 5d, curve 3) is related to a composite-like effect due to inhomogeneous reduction of the sample.

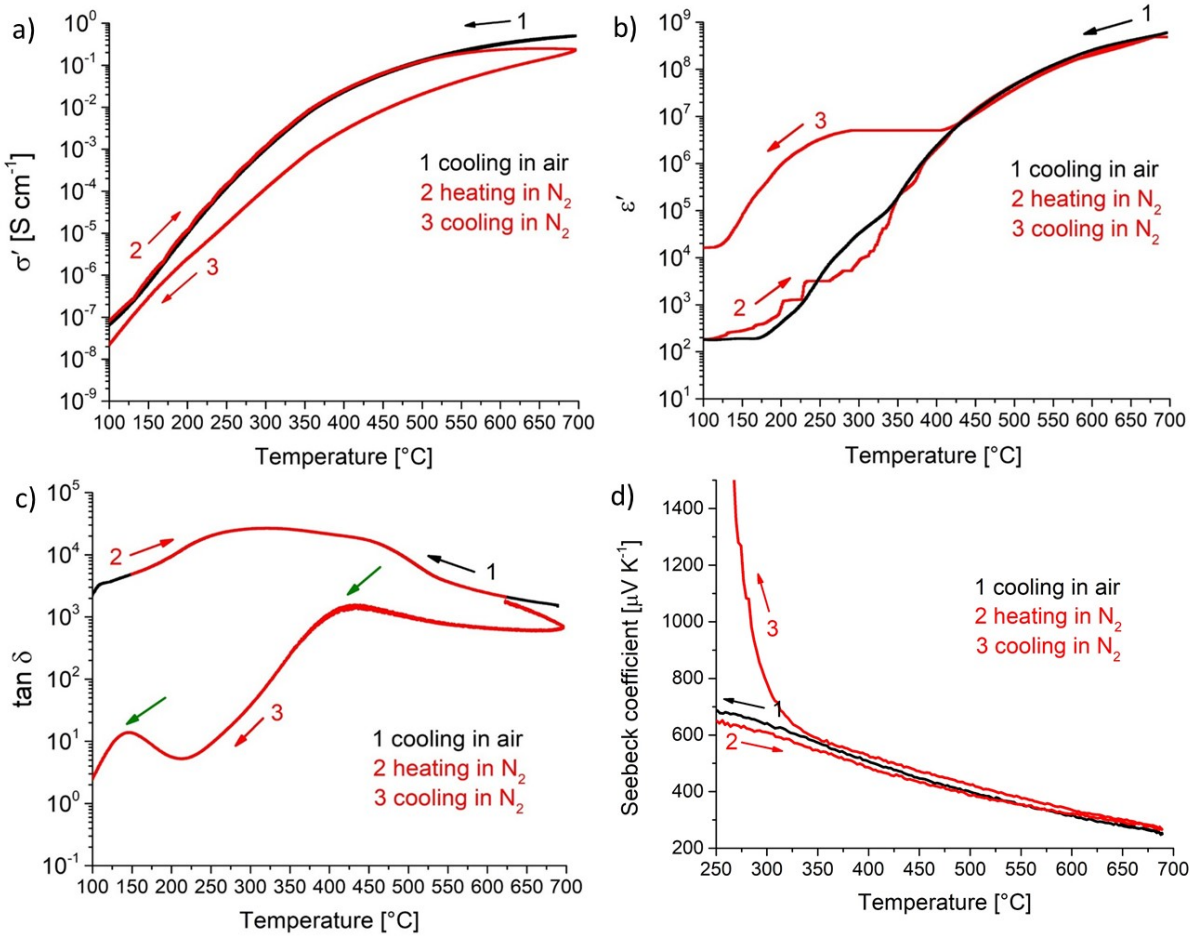

Figure 5: a) σ′ , b) ε′, c) tan δ and d) Seebeck coefficient as a function of temperature and annealing atmosphere for 1.5 at% Co doped BFO ceramics. Curves 1, 2 and 3 correspond to cooling in air, heating in N_2 and cooling in N_2, respectively. Green arrows in c) indicate peak in tan δ.

The results presented so far, i.e., permittivity measurements at room temperature (Figure 4), isothermal DC conductivity measurements (Supplementary material, Fig. S2) and *in-situ* measurements of AC conductivity and Seebeck coefficient (Figure 5), indicate localized redox processes, which may preferentially occur along grain boundaries and/or domain walls [17]. This possibility is investigated more in detail in the next section.

3.4 Insight into the locations and type of point defects

In order to investigate conductivity of grain boundaries (GBs) and domain walls (DWs), local conductivity measurements were performed using conductive atomic-force microscopy (c-AFM) combined with piezo-response force microscopy (PFM) for GB and DW identification. Figure 6 shows the results for as-sintered and N_2-annealed samples of 1.5 at% Co doped BFO ceramics. Note that while these are representative images, a more rigorous statistical analysis on the fraction of conductive DWs and GBs was done and is presented later.

In the as-sintered sample, an enhanced current signal can be observed in several regions (Figure 6b), which were identified as DWs (denoted by green arrows) and GBs (denoted by red arrows) with PFM (Figure 6a). The increased current signal at these interfaces is clearly confirmed by the c-AFM profiles shown in Figure 6c,d.

After annealing in N_2, a similar PFM and c-AFM analysis was performed as shown in Figure 6e-h. The relative amount of GBs and DWs with enhanced local conductivity is reduced (Figure 6f) with respect to the as-sintered sample (Figure 6b). To corroborate these results, a statistical analysis of the local current at GBs and DWs was performed. Multiple areas in as-sintered and N_2-annealed samples were analyzed with c-AFM, probing a total of ~140 grains and ~180 DWs per sample. Afterwards, the fractions of GBs and DWs that were accompanied by the enhanced current signal were determined. The fractions of conductive GBs were 26 % and 17 % and of conductive DWs were 49 % and 26 % for as-sintered and N_2-annealed samples, respectively. While the difference in the fractions of conductive GBs between as-sintered and N_2 samples is smaller than that of conductive DWs, in average, we can conclude that the conductivity of the analyzed interfaces is reduced after annealing in N_2, in accordance with Eq. 1.3. This is related to the local reduction of the major charge carriers, Fe^{4+}, by N_2 annealing.

These findings are in agreement with the recent study by Rojac *et* al. [17], where the origin of DW conduction was attributed to Fe^{4+} and the reduction of DWs conductivity after annealing in N_2 to reduction of Fe^{4+} into Fe^{3+}. Note, however, that the difference in fractions of conductive DWs between as-sintered and N_2-annealed samples in ref. [17] were much more prominent (84 % vs 3 %), which could be related to different processing conditions resulting in different charge distributions and annealing conditions.

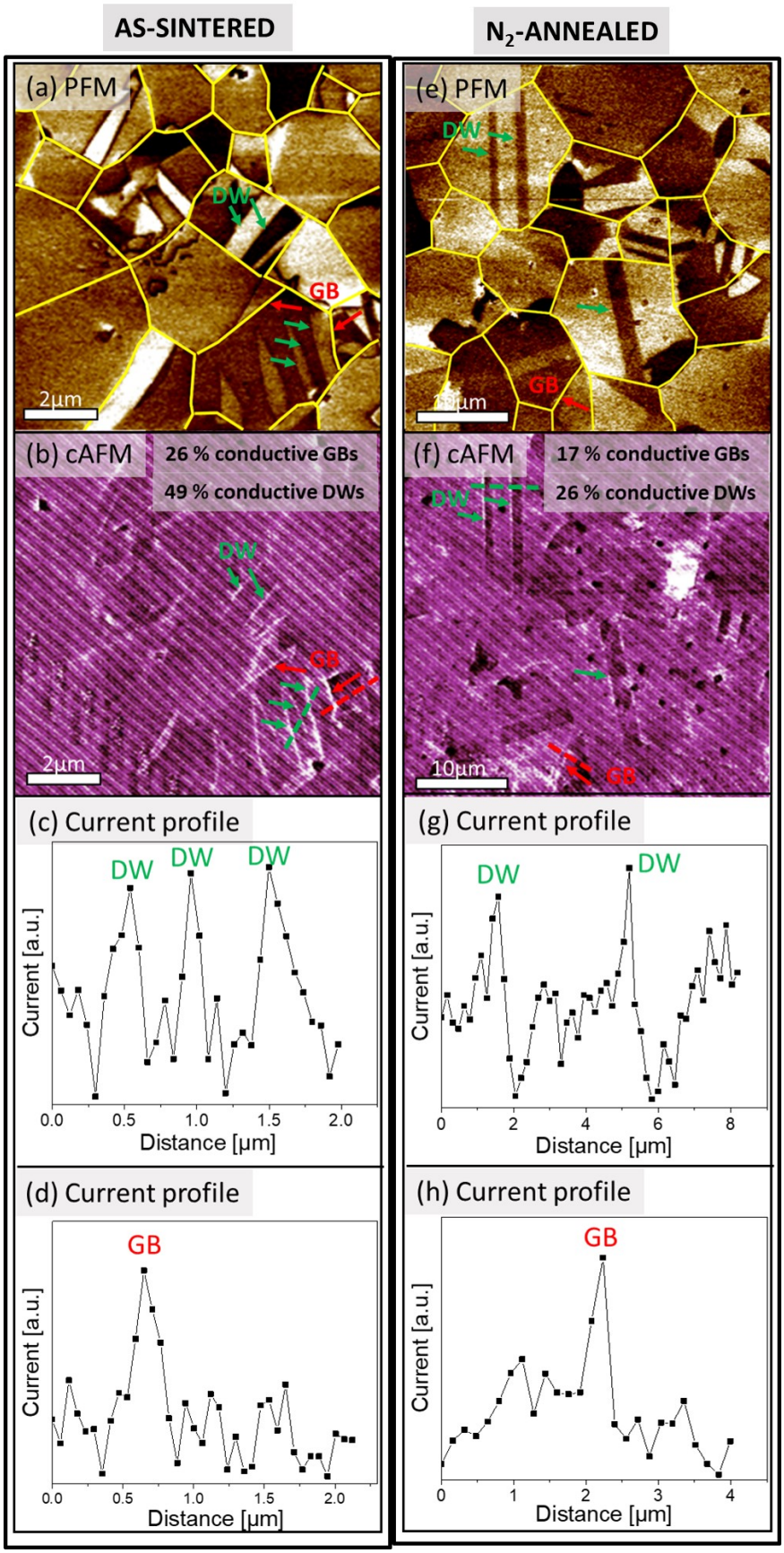

Figure 6: (a,e) Out-of-plane PFM images, (b,f) c-AFM maps and (c-h) electric-current profiles corresponding to as-sintered and N_2-annealed sample of 1.5 at% Co doped BFO ceramics. Yellow lines in PFM images mark the grain boundaries. The green and red arrows in the PFM and c-AFM

images denote those DWs and GBs, respectively, where the enhanced electric current-signal was clearly observed by c-AFM. The green and arrow dashed lines in the c-AFM images correspond to the distance along which the electric-current profiles, shown in panels (c-h), were extracted. The DW and GB positions along this distance are indicated on the profiles (DW-domain wall, GB-grain boundary).

The three different samples of 1.5 at% Co doped BFO ceramics, i.e., as-sintered, N_2-annealed and 10-atm-O_2-annealed (Figure 3 and Figure 4) were analyzed using electron paramagnetic resonance (EPR). The corresponding X-band spectra are presented in Figure 7. The spectra shown here were obtained above Neel temperature (T_N = 370 °C) [10], i.e., at 400 °C, in order to avoid contributions of static internal fields due to antiferromagnetic ordering and therefore, to observe intrinsic contributions (see Supplementary material, Fig. S4a). Starting from as-sintered sample, an anisotropic spectrum with g_x = 1.80, g_y = 3.13 and g_z = 2.36 was found by numerical spectrum simulations (for more details see Supplementary material, Fig. S4b and Table S1). The g values for N_2- and 10-atm-O_2-annealed samples were g_x = 1.82, g_y = 2.90, g_z = 2.28 and g_x = 2.23, g_y = 3.38 and g_z = 1.84, respectively. Similar values were reported in the literature for low-spin Co^{2+} in square planar or pseudo-tetrahedral geometry [54,55]. In case of Co doped BFO, we reasonably assume that Co occupies B site in the perovskite structure and is surrounded by oxygen octahedra. The g values observed indicate the presence of Co^{2+} ions placed in tetrahedron of oxygen ions. This could be interpreted in terms of the presence of Co^{2+} surrounded by $V_O^{\bullet\bullet}$ and thus $Co'_{Fe} - V_O^{\bullet\bullet}$ defect complexes. According to the literature data, these g values could be alternatively attributed to high-spin Co^{2+} in the distorted tetrahedral geometry, which is again consistent with the presence of $V_O^{\bullet\bullet}$ residing in the vicinity of Co^{2+} [56]. The identification of Co^{2+} is in agreement with ref. [47] on Co-doped BFO thin films sintered in O_2 flow, where it was found by X-ray photoelectron spectroscopy that Co ions are mostly in oxidation state 2+ (smaller fraction is in the form 3+). Furthermore, the existence of cobalt-oxygen-vacancy defect complexes has been reported in DFT study on Co-doped $SrTiO_3$ (STO), with a linear arrangement of $Co''_{Ti} - V_O^{\bullet\bullet}$ being energetically favored [57].

The intensity of EPR signal is directly proportional to the relative numbers of unpaired electrons in the sample. In this study, the masses of the powders were comparable in all cases, which means that the intensity of EPR signal can be directly linked to defect concentration. If the observed signal is indeed related to $Co'_{Fe} - V_O^{\bullet\bullet}$ type of defects, the highest intensity should be seen in N_2 and the lowest in O_2-annealed sample, which is indeed observed experimentally (Figure 7). These results therefore suggest that the concentration of $Co'_{Fe} - V_O^{\bullet\bullet}$ defect complexes is increased by annealing in N_2 and decreased by annealing in O_2, relative to the as-

sintered sample, The increased concentration of $Co'_{Fe} - V_O^{\bullet\bullet}$ defect complexes could be related to reduction of Co^{3+} into Co^{2+} and the formation of $V_O^{\bullet\bullet}$ considering that the as-sintered sample most likely contains a mixture of Co^{3+} and Co^{2+} [47]. Another possibility for the increased concentration of $Co'_{Fe} - V_O^{\bullet\bullet}$ defect complexes is by formation of $V_O^{\bullet\bullet}$ due to reduction of Fe^{4+} into Fe^{3+}, which then diffuse close to Co^{2+} ions as $V_O^{\bullet\bullet}$ should be attracted to acceptor centers.

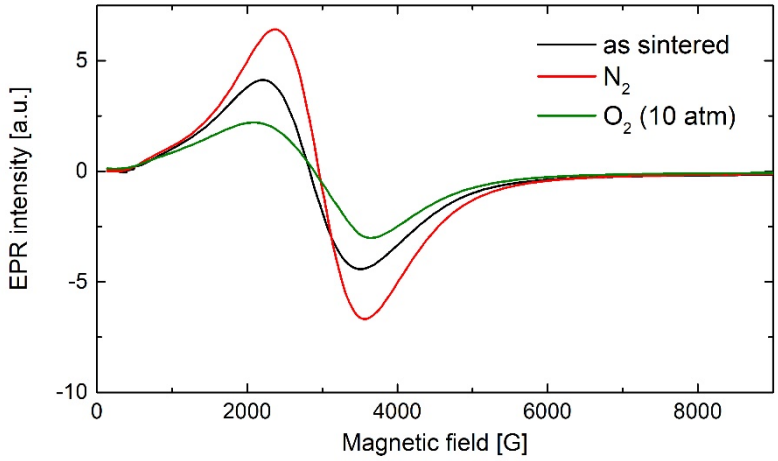

Figure 7: Electron paramagnetic resonance (EPR) measurements of as-sintered, N_2- and 10-atm-O_2-annealed sample of 1.5 at% Co doped BFO composition.

3.5 Proposed defect and hardening mechanism for Co-doped BFO ceramics

In the current study, it has been found that by increasing the concentration of Co, electrical conductivity increases (see Figure 2) as well as the hysteresis loop pinching (hardening) (Figure 1). As a result, it has been assumed that Co acts as acceptor, promoting the formation of $V_O^{\bullet\bullet}$ (equation (3.2) and $Fe_{Fe}^{\bullet}$ (equation (1.3)). For this case, the charge neutrality condition can be expressed as

$$3[V_{Bi}'''] + [Co'_{Fe}] = 2[V_O^{\bullet\bullet}] + [Fe_{Fe}^{\bullet}] \tag{3.5}$$

In 1.5 at% Co doped BFO ceramics, the high concentration of extrinsic Co'_{Fe} and $V_O^{\bullet\bullet}$ probably dominates over intrinsic V_{Bi}''', $V_O^{\bullet\bullet}$ and $Fe_{Fe}^{\bullet}$. In addition, we can infer that the concentration of V_{Bi}''' is freezed-in at lower temperatures (<700°C) by the quasi-equilibrium achieved during sintering and is not altered by the post-annealing in N_2, as it has been shown that the redox processes occurring in N_2 are reversible by O_2 annealing (see Supplementary material, Fig.

S3). While the major contribution to elevated p-type electrical conductivity is due to $Fe_{Fe}^{\bullet}$, based on the literature data and the results of this study, we assume there are two types of pinning centers, i.e., those related to V_{Bi}''' and $Fe_{Fe}^{\bullet}$ that have a tendency to accumulate at DWs [17] from which they can provide pinning effects, and to Co_{Fe}' and $V_O^{\bullet\bullet}$ (EPR results in Figure 7), which most likely bind into complexes. The question then becomes if and which defect(s) dominates the DW pinning behavior at switching electric fields (hysteresis pinching).

We found that annealing in N_2 results in strongly impeded polarization switching (Figure 3). The reduction in N_2 occurs locally, as evidenced by the relaxation in ε' at RT (Figure 4a) and at elevated temperatures (Figure 5b), increased Seebeck coefficient at lower temperatures (Figure 5d) and fast redox kinetics (Supplementary material, Fig. S2). Moreover, annealing in N_2 results in reduced fraction of conductive GBs and DWs (c-AFM analysis in Figure 6), which is related to the reduction of Fe^{4+} into Fe^{3+} at these local regions of the sample. Therefore, it can be concluded that the concentration of $Fe_{Fe}^{\bullet}$-related pinning centers is lowered the most after annealing in N_2 and thus cannot explain the stronger pinning behavior of N_2-annealed BFO. We leave open the possibility, however, that the different switching behavior after annealing in N_2 might be affected by the internal field distribution inside the grain matrix related to the M-W effects. In contrast, it has been found that the concentration of $Co_{Fe}' - V_O^{\bullet\bullet}$ complexes increases after annealing in N_2 (EPR results in Figure 7), suggesting that the strong hardening induced by N_2 annealing originates from an increased concentration of $Co_{Fe}' - V_O^{\bullet\bullet}$ pinning centers.

Relative to the as-sintered sample, annealing in 10 atm O_2 results in facilitated polarization switching (Figure 3), with small changes observed in the electrical conductivity (Figure 4c). Considering that the p-type conductivity in BFO is dominated by $Fe_{Fe}^{\bullet}$, the conductivity behavior indicates that the concentration of $Fe_{Fe}^{\bullet}$ was only subtly affected by the annealing in 10 atm O_2. Thus, assuming a quasi-constant concentration of $Fe_{Fe}^{\bullet}$ and V_{Bi}''', the latter fixed at the sintering conditions (see earlier discussion), the concentration of Co_{Fe}' must have been reduced in order to satisfy the charge neutrality condition as the concentration of $V_O^{\bullet\bullet}$ has been decreased. This suggests that Co^{2+} is (partially) oxidized to Co^{3+}. Furthermore, this scenario is in agreement with EPR results (Figure 7), which show reduced concentration of $Co_{Fe}' - V_O^{\bullet\bullet}$ complexes after annealing in 10 atm O_2.

Finally, considering the totality of the results it can be concluded that pinching (hardening) in 1.5 at% Co doped BFO ceramics, as evidenced by the high-field polarization hysteresis

loops, is dominated by $\mathrm{Co}'_{\mathrm{Fe}} - \mathrm{V}_{\mathrm{O}}^{\bullet\bullet}$ defect complexes. We point out that qualitatively similar behavior as found in 1.5 at% Co doped ceramics has also been observed in the composition containing 0.25 at% Co (Supplementary material, Fig. S5 and Fig. S6). This suggests that the proposed pinning mechanisms applies to a wide Co concentration range (0.25 – 1.5 at% Co).

4 Summary and conclusions

In this report, the influence of cobalt doping and annealing atmosphere on defect chemistry, electrical conductivity and polarization switching of BFO ceramics was studied. We found that by increasing the Co concentration, the conductivity and hardening increases, as observed from pinched and bias hysteresis loops. This is attributed to increased concentration of $Fe_{Fe}^{\bullet}$ and $V_O^{\bullet\bullet}$ due to the introduction of Co acceptor dopants on Fe sites; Co'_{Fe}.

It has been shown that the conductivity decreases in N_2, confirming p-type conductive behavior. The fast redox kinetics upon isothermally switching atmosphere between O_2 and N_2 gave an indication of local redox reactions, occurring predominantly on grain boundaries and at domain walls, as confirmed by the local c-AFM measurements. This was further supported by the observation of Maxwell-Wagner relaxation during cooling in N_2. Most importantly, while the p-type conductivity is dominated by Fe^{4+} defects, $Co'_{Fe} - V_O^{\bullet\bullet}$ complexes, identified by EPR, were shown to play the key role in the hardening behavior and hysteresis loop pinching and biasing. We hope that the results presented here will contribute to a better understanding of defect chemistry in BFO-related materials and assist a further design of functional properties through hardening by acceptor doping.

Acknowledgements

The authors would like to thank Damjan Vengust for his help with sample preparation and Tjaša Klavžar for c-AFM/PFM analysis. The work was financially supported by the Slovenian Research Agency (young researcher project PR-08350 and research core funding P2-0105) and JECS Trust (Contract No. 2017298). DRS and SMS were supported by the Research Council of Norway through project 231430.

References

[1] A. Pramanick, D. Damjanovic, J.E. Daniels, J.C. Nino, J.L. Jones, Origins of electromechanical coupling in polycrystalline ferroelectrics during subcoercive electrical loading, J. Am. Ceram. Soc. 94 (2011) 293–309. doi:10.1111/j.1551-2916.2010.04240.x.

[2] L.E. Cross, Ferroelectric materials for electromechanical applications, Mater. Chem. Phys. 43 (1996) 108–115.

[3] A. Chandrasekaran, D. Damjanovic, N. Setter, N. Marzari, Defect ordering and defect-domain-wall interactions in PbTiO 3: A first-principles study, Phys. Rev. B - Condens. Matter Mater. Phys. 88 (2013) 1–9. doi:10.1103/PhysRevB.88.214116.

[4] P. Erhart, P. Traskelin, K. Albe, Formation and switching of defect dipoles in acceptor-doped lead titanate: A kinetic model based on first-principles calculations, Phys. Rev. B - Condens. Matter Mater. Phys. 88 (2013) 1–10. doi:10.1103/PhysRevB.88.024107.

[5] W.L. Warren, D. Dimos, G.E. Pike, K. Vanheusden, R. Ramesh, Alignment of defect dipoles in polycrystalline ferroelectrics, Appl. Phys. Lett. 67 (1995) 1689. doi:10.1063/1.115058.

[6] L.X. Zhang, X. Ren, In situ observation of reversible domain switching in aged Mn-doped BaTiO3 single crystals, Phys. Rev. B - Condens. Matter Mater. Phys. 71 (2005) 1–8. doi:10.1103/PhysRevB.71.174108.

[7] H. Jaffe, B., Cook, W.R.J., Jaffe, Piezoelectric Ceramics, US, Academic Press, New York, 1971.

[8] J. Rödel, W. Jo, K.T.P. Seifert, E.M. Anton, T. Granzow, D. Damjanovic, Perspective on the development of lead-free piezoceramics, J. Am. Ceram. Soc. 92 (2009) 1153–1177. doi:10.1111/j.1551-2916.2009.03061.x.

[9] T. Stevenson, D.G. Martin, P.I. Cowin, a. Blumfield, a. J. Bell, T.P. Comyn, P.M. Weaver, Piezoelectric materials for high temperature transducers and actuators, J. Mater. Sci. Mater. Electron. 26 (2015) 9256–9267. doi:10.1007/s10854-015-3629-4.

[10] G. Catalan, J.F. Scott, Physics and Applications of Bismuth Ferrite, Adv. Mater. 21 (2009) 2463–2485. doi:10.1002/adma.200802849.

[11] J. Seidel, P. Maksymovych, Y. Batra, a. Katan, S.Y. Yang, Q. He, a. P. Baddorf, S. V. Kalinin, C.H. Yang, J.C. Yang, Y.H. Chu, E.K.H. Salje, H. Wormeester, M. Salmeron, R. Ramesh, Domain wall conductivity in La-doped BiFeO3, Phys. Rev. Lett. 105 (2010) 2010–2012. doi:10.1103/PhysRevLett.105.197603.

[12] S. Farokhipoor, B. Noheda, Local conductivity and the role of vacancies around twin walls of (001)-BiFeO 3 thin films, J. Appl. Phys. 112 (2012). doi:10.1063/1.4746073.

[13] S. Farokhipoor, B. Noheda, Conduction through 71??domain walls in BiFeO3 thin films, Phys. Rev. Lett. 107 (2011) 3–6. doi:10.1103/PhysRevLett.107.127601.

[14] Z. Zhang, P. Wu, L. Chen, J. Wang, Z. Zhang, P. Wu, L. Chen, J. Wang, Density functional theory plus U study of vacancy formations in bismuth ferrite Density functional theory plus U study of vacancy formations in bismuth ferrite, 232906 (2010) 210–213. doi:10.1063/1.3447369.

[15] T.R. Paudel, S.S. Jaswal, E.Y. Tsymbal, Intrinsic defects in multiferroic BiFeO 3 and their effect on magnetism, 104409 (2012) 1–8. doi:10.1103/PhysRevB.85.104409.

[16] N. Maso, A.R. West, Electrical Properties of Ca-Doped BiFeO 3 Ceramics: From p - Type Semiconduction to Oxide-Ion Conduction, (2012).

[17] T. Rojac, A. Bencan, G. Drazic, N. Sakamoto, H. Ursic, B. Jancar, G. Tavcar, M. Makarovic, J. Walker, B. Malic, D. Damjanovic, Domain-wall conduction in ferroelectric BiFeO 3 controlled by accumulation of charged defects, Nat. Mater. 16 (2017). doi:10.1038/nmat4799.

[18] T. Rojac, A. Bencan, B. Malic, G. Tutuncu, J.L. Jones, J.E. Daniels, D. Damjanovic, BiFeO 3 Ceramics: Processing, Electrical, and Electromechanical Properties, J. Am. Ceram. Soc. 97 (2014) 1993–2011. doi:10.1111/jace.12982.

[19] E.T. Wefring, M. Einarsrud, T. Grande, Electrical conductivity and thermopower of phase transition, Phys. Chem. Chem. Phys. 17 (2015) 9420–9428. doi:10.1039/C5CP00266D.

[20] G.L. Yuan, Y. Yang, S.W. Or, Aging-induced double ferroelectric hysteresis loops in BiFeO3 multiferroic ceramic, Appl. Phys. Lett. 91 (2007) 2005–2008. doi:10.1063/1.2786013.

[21] T. Rojac, M. Kosec, B. Budic, N. Setter, D. Damjanovic, Strong ferroelectric domain-wall pinning in BiFeO3 ceramics, J. Appl. Phys. 108 (2010) 0–8. doi:10.1063/1.3490249.

[22] R.-A. Eichel, Structural and dynamic properties of oxygen vacancies in perovskite oxides — analysis of defect chemistry by modern multi-frequency and pulsed EPR techniques, Phys. Chem. Chem. Phys. 13 (2011) 368–384. doi:10.1039/b918782k.

[23] M.I. Morozov, D. Damjanovic, Charge migration in Pb(Zr,Ti)O3 ceramics and its relation to ageing, hardening, and softening, J. Appl. Phys. 107 (2010) 0–10. doi:10.1063/1.3284954.

[24] F. Chen, Q.F. Zhang, J.H. Li, Y.J. Qi, C.J. Lu, X.B. Chen, X.M. Ren, Y. Zhao, Sol-gel derived multiferroic BiFeO3 ceramics with large polarization and weak ferromagnetism, Appl. Phys. Lett. 89 (2006) 210–213. doi:10.1063/1.2345603.

[25] Y.P. Wang, L. Zhou, M.F. Zhang, X.Y. Chen, J. Liu, Z.G. Liu, Y.P. Wang, L. Zhou, M.F. Zhang, X.Y. Chen, J. Liu, Z.G. Liu, Room-temperature saturated ferroelectric polarization in by rapid liquid phase sintering Room-temperature saturated ferroelectric polarization in BiFeO 3 ceramics synthesized by rapid liquid phase sintering, 1731 (2005) 1–4. doi:10.1063/1.1667612.

[26] X. Qi, J. Dho, R. Tomov, Greatly reduced leakage current and conduction mechanism in aliovalent-ion- doped BiFeO3, Appl. Phys. Lett. 86 (2005). doi:10.1063/1.1862336.

[27] V.A. Khomchenko, D.A. Kiselev, M. Kopcewicz, M. Maglione, V. V Shvartsman, P. Borisov, W. Kleemann, A.M.L. Lopes, Y.G. Pogorelov, J.P. Araujo, R.M. Rubinger, N.A. Sobolev, J.M. Vieira, A.L. Kholkin, Doping strategies for increased performance in BiFeO 3, J. Magn. M. 321 (2009) 1692–1698. doi:10.1016/j.jmmm.2009.02.008.

[28] M. Kumar, K.L. Yadav, G.D. Varma, Large magnetization and weak polarization in sol – gel derived BiFeO 3 ceramics, Mater. Le. 62 (2008) 1159–1161. doi:10.1016/j.matlet.2007.07.075.

[29] Y. Yoneda, W. Sakamoto, Electronic and local structures of BiFeO 3, J. Phys. Condens. Matter. 23 (2011). doi:10.1088/0953-8984/23/1/015902.

[30] M. Schrade, N. Maso, A. Perejón, L. Perez-Maqueda, A.R. West, Defect chemistry and electrical properties of BiFeO3, J. Mater. Chem. C. 5 (2017) 10077–10086.

doi:10.1039/C7TC03345A.

[31] Z. Dai, Y. Akishige, BiFeO 3 ceramics synthesized by spark plasma sintering, Ceram. Int. 38S (2012) S403–S406. doi:10.1016/j.ceramint.2011.05.020.

[32] E. Wefring, K.G. Webber, M.-A. Einarsrud, Electrical conductivity and ferroelastic properties of Ti-substituted solid solutions (1-x)BiFeO3-xBi0.5K0.5TiO3, Jpurnal Eur. Ceram. Soc. 36 (2016) 497–506. doi:10.1016/j.jeurceramsoc.2015.09.044.

[33] M.I. Morozov, M.-A. Einarsrud, T. Grande, Atmosphere controlled conductivity and Maxwell-Wagner relaxation in Bi0.5K0.5TiO3—BiFeO3 ceramics, J. Appl. Phys. 115 (2014) 44104. doi:10.1063/1.4863798.

[34] A.R. Makhdoom, M.J. Akhtar, R.T.A. Khan, M.A. Ra, M.M. Hasan, F. Sher, A.N. Fitch, Association of microstructure and electric heterogeneity in BiFeO 3, 143 (2013) 256–262. doi:10.1016/j.matchemphys.2013.08.061.

[35] A.Y. Kim, Y.J. Lee, J.S. Kim, Ferroelectric Properties of BiFeO 3 Ceramics Sintered under Low Oxygen Partial Pressure, 60 (2012) 83–87. doi:10.3938/jkps.60.83.

[36] C. Paillard, B. Dkhil, Polarons, vacancies, vacancy associations and defect states in multiferroic BiFeO 3, (2018) 1–20.

[37] T. Rojac, H. Ursic, A. Bencan, B. Malic, D. Damjanovic, Mobile domain walls as a bridge between nanoscale conductivity and macroscopic electromechanical response, Adv. Funct. Mater. 25 (2015) 2099–2108. doi:10.1002/adfm.201402963.

[38] J. Seidel, L.W. Martin, Q. He, Q. Zhan, A. Rother, M.E. Hawkridge, P. Maksymovych, P. Yu, M. Gajek, N. Balke, S. V Kalinin, S. Gemming, F. Wang, G. Catalan, J.F. Scott, N.A. Spaldin, J. Orenstein, R. Ramesh, Conduction at domain walls in oxide multiferroics, Nat. Mater. 8 (2009) 229–234. doi:10.1038/nmat2373.

[39] TOPAS version 2.1, Bruker AXS, (n.d.). www.bruker-axs.com.

[40] Y.A. Genenko, J. Glaum, M.J. Hoffmann, K. Albe, Mechanisms of aging and fatigue in ferroelectrics, Mater. Sci. Eng. B Solid-State Mater. Adv. Technol. 192 (2015) 52–82. doi:10.1016/j.mseb.2014.10.003.

[41] I. Wærnhus, P. Erik, R. Holmestad, T. Grande, K. Wiik, Electronic properties of polycrystalline LaFeO 3 . Part I : Experimental results and the qualitative role of

Schottky defects, Solid State Ionics. 176 (2005) 2783–2790. doi:10.1016/j.ssi.2005.08.012.

[42] G.L. Yuan, S.W. Or, Y.P. Wang, Z.G. Liu, J.M. Liu, Preparation and multi-properties of insulated single-phase BiFeO 3 ceramics, Solid State Commun. 138 (2006) 76–81. doi:10.1016/j.ssc.2006.02.005.

[43] T. Rojac, M. Kosec, B. Budic, N. Setter, D. Damjanovic, Strong ferroelectric domain-wall pinning in BiFeO[sub 3] ceramics, J. Appl. Phys. 108 (2010) 74107. doi:10.1063/1.3490249.

[44] K. Carl, K.H. Hardtl, Electrical after-effects in Pb(Zr,Ti)O3 ceramics, Ferroelectrics. 17 (1978) 476–486.

[45] A.K. Jonscher, Dielectric Relaxation in Solids, Chelsea Dielectrics Press Limited, London, 1983.

[46] Y. Chiang, C. Tu, P. Chen, C. Chen, J. Anthoniappen, Y. Ting, T. Chan, V.H. Schmidt, Magnetic and phonon transitions in B-site Co doped BiFeO 3 ceramics, Ceram. Int. 42 (2016) 13104–13112. doi:10.1016/j.ceramint.2016.05.097.

[47] N.S. Bein, P. Machado, M. Coll, F. Chen, M. Makarovic, T. Rojac, A. Klein, Electrochemical Reduction of Undoped and Cobalt-Doped BiFeO3 Induced by Water Exposure: Quantitative Determination of Reduction Potentials and Defect Energy Levels Using Photoelectron Spectroscopy, J. Phys. Chem. Lett. 10 (2019) 7071–7076. doi:10.1021/acs.jpclett.9b02706.

[48] T. Rojac, M. Makarovic, J. Walker, H. Ursic, D. Damjanovic, T. Kos, Piezoelectric response of BiFeO3 ceramics at elevated temperatures Piezoelectric response of BiFeO 3 ceramics at elevated temperatures, 42904 (2016) 1–5. doi:10.1063/1.4960103.

[49] P. Lunkenheimer, V. Bobnar, A. V Pronin, A.I. Ritus, A.A. Volkov, A. Loidl, Origin of apparent colossal dielectric constants, Phys. Rev. B. 66 (2002) 52105. doi:10.1103/PhysRevB.66.052105.

[50] N. Masó, A.R. West, Electrical Properties of Ca-Doped BiFeO 3 Ceramics: From p - Type Semiconduction to Oxide-Ion Conduction, Chem. Mater. 24 (2012) 2127–2132. doi:10.1021/cm300683e.

[51] M.I. Morozov, M.A. Einarsrud, T. Grande, Control of conductivity and electric field

induced strain in bulk Bi 0.5K0.5TiO3-BiFeO3 ceramics, Appl. Phys. Lett. 104 (2014) 0–4. doi:10.1063/1.4869976.

[52] J. Mizusaki, T. Sasamoto, R. Cannon, K. Bowen, Electronic Conductivity, Seebeck Coefficient, and Defect structure of La1-xSrxFeO3 (x=0.1, 0.25), J. Am. Ceram. Soc. 66 (1983) 247–252.

[53] H. Ju, J. Kim, Chemically Exfoliated SnSe Nanosheets and Their SnSe/Poly(3,4-ethylenedioxythiophene):Poly(styrenesulfo nate) Composite Films for Polymer Based Thermoelectric Applications, ACS Nano. 10 (2016) 5730–5739. doi:10.1021/acsnano.5b07355.

[54] S. Hoffman, J. Goslar, S. Lijewski, Electron Paramagnetic Resonance and Electron Spin Echo Studies of Co 2 + Coordination by Nicotinamide Adenine Dinucleotide (NAD +) in Water Solution, Appl. Magn. Reson. 44 (2013) 817–826. doi:10.1007/s00723-013-0444-z.

[55] D.M. Jenkins, A.J. Di Bilio, M.J. Allen, T.A. Betley, J.C. Peters, Elucidation of a Low Spin Cobalt (II) System in a Distorted Tetrahedral Geometry, J. Am. Chem. Soc. 124 (2002) 15336–15350. doi:10.1021/ja026433e.

[56] H. Drulis, K. Dyrek, K.P. Hoffmann, S.K. Hoffmann, A. Weselucha-Birczynska, EPR Spectra of Low-Symmetry Tetrahedral High-Spin Cobalt (II) in a Cinchoninium Tetrachlorocobaltate (II) Dihydrate Single Crystal, Inorg. Chem. 24 (1985) 4009–4012. doi:10.1021/ic00218a009.

[57] C. Mitra, C. Lin, A.B. Posadas, A.A. Demkov, Role of oxygen vacancies in room-temperature ferromagnetism in cobalt-substituted SrTiO3, Phys. Rev. B. 90 (2014) 125130. doi:10.1103/PhysRevB.90.125130.

Supplementary material

Figure S1. Structure and phase composition of Co-doped BFO ceramics

In Fig. S 1 the diffraction patterns of BFO doped with different concentration of Co are shown. The major phase in all compositions is the perovskite phase (p). The extra peak with low intensity at 2θ = 28° can be attributed to $Bi_{25}FeO_{40}$ (sillenite phase) secondary phase (denoted with *, see inset). The intensity of this peak is similar in all compositions, meaning that the amount of the secondary sillenite phase is comparable between the different samples. This was confirmed quantitatively by Rietveld refinement of the XRD patterns displayed here, which showed that the amount of the sillenite phase in all the samples does not exceed ~1 wt.%. While the effects of the uncompleted reaction and the possible resulting substiochiometric BFO on the electrical conductivity and domain switching behavior cannot be ruled out a priori, we note that a comparable concentration of secondary phases in these samples still allows to clearly assess the effect of the dopant.

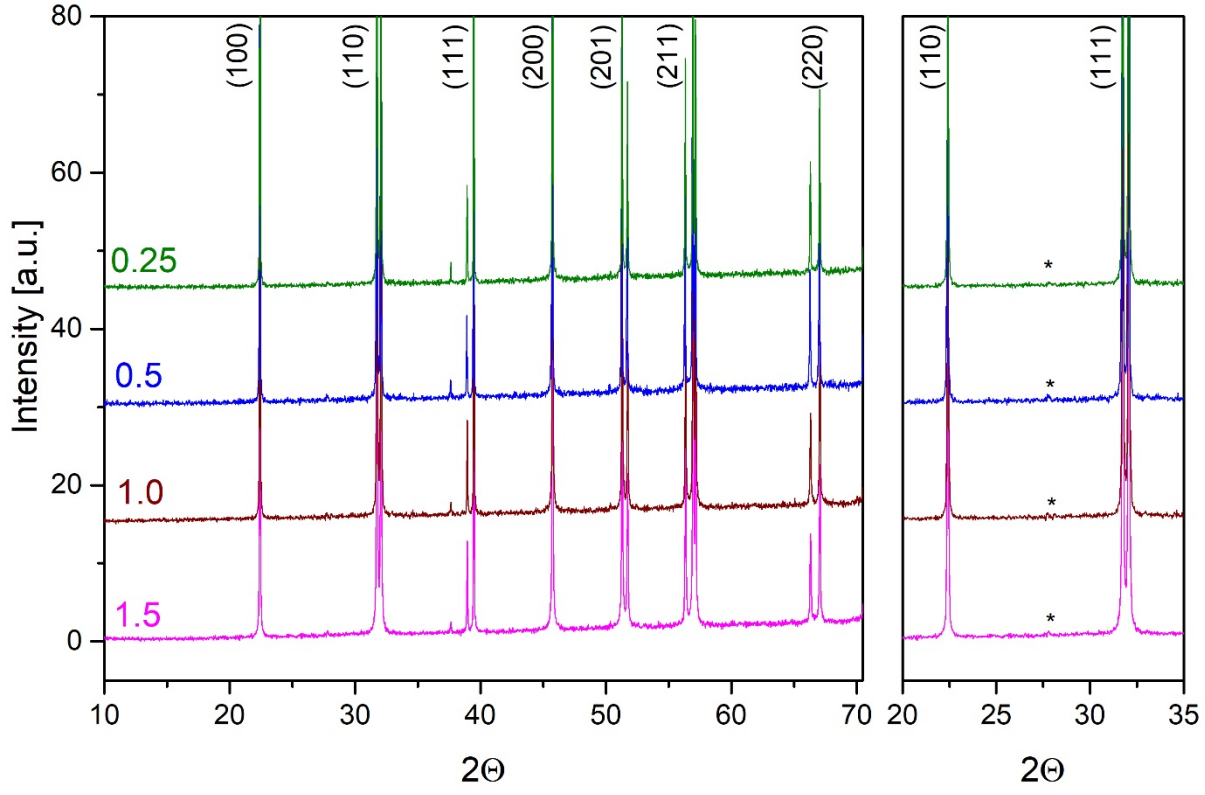

Fig. S 1: XRD patterns of BFO ceramics doped with 0.25, 0.5, 1.0 and 1.5 at% Co. The peaks of the perovskite phase are labelled according to pseudo-cubic notation. The inset shows an enlarged part of the pattern, highlighting the weak peak of the secondary phase, appearing just above the background signal (= sillenite phase, $Bi_{25}FeO_{40}$).*

Figure S2. Isothermal DC conductivity measurements of 1.5 at% Co doped ceramics

In order to get an insight into redox kinetics and possibly explain the local nature of the reduction in N_2, leading to the relaxation in the permittivity data (see paper, Figure 4), isothermal DC conductivity measurements were performed at 600 °C upon changing the atmosphere between O_2 and N_2. As it can be observed in Fig. S 2, the conductivity decreases upon switching the atmosphere from O_2 to N_2 and increases again upon switching from N_2 to O_2. This is consistent with p-type behavior of BFO. Moreover, it can be seen that the relaxation time under reduced $p(O_2)$ (i.e., switch from O_2 to N_2) and increased $p(O_2)$ (i.e., switch from N_2 to O_2), appears to be extremely fast, i.e., in the order of minutes.

Fast redox kinetics has been observed in hexagonal manganites [S1] due to highly mobile interstitial oxygen ions. The close-packed structure of BFO, however, is not favorable for interstitial defects. In addition, fast redox kinetics cannot be simply attributed to microstructural origins, e.g., porosity, as the BFO samples exhibited high relative density (~93%) (see inset in Fig. S 2). Another possibility to explain the fast conductivity relaxation is that the redox processes occur at the surface of the sample. We note, however, that a decrease of electrical conductivity, i.e., reduction in N_2, has been observed also in permittivity measurements performed at room temperature (see paper, Figure 4), where the surface layer with a few hundred microns was removed prior to analysis. A final possibility are localized redox processes occurring along on grain boundaries and/or domain walls; the latter has been recently reported by Rojac et al. [S2].

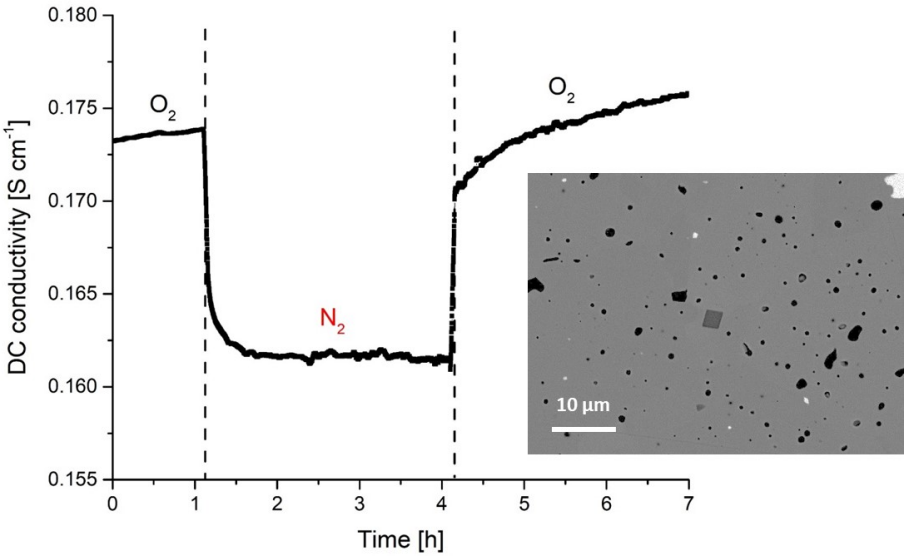

Fig. S 2: Relaxation of conductivity upon switching between O_2 and N_2 at 600 °C for 1.5 at% Co doped BFO ceramics. The inset shows scanning electron microscope (SEM) image of polished 1.5 at% Co

doped BFO ceramics used for DC conductivity measurements, highlighting the relatively high density (~93%) of the sample. The bright, brown and black regions are sillenite phase, mullite phase and pores, respectively.

Figure S3. Reversibility of redox reaction in 1.5 at% Co doped ceramics

In order to confirm that the changes observed the AC conductivity and Seebeck coefficient (see paper, Figure 5) after annealing in N_2 are reversible, the samples were re-annealed in air. The results are presented in Fig. S 3, where the curves labeled 1-5 refer to cooling cycle in air, heating cycle in N_2, cooling cycle in N_2, heating cycle in air (after N_2) and cooling cycle in air (after N_2), respectively. The cycles 1-3 and the associated changes have already been discussed in the paper (see Figure 5 and text for explanation).

In Fig. S 3a, σ' measured at 1 Hz is presented. It can be observed that upon re-annealing in air (4), the curve traces that measured in N_2 during cooling (3) only up to ~275 °C and afterwards deviates from the trend measured in N_2 (compare curves 3 and 4 above 275 °C). Moreover, it can be observed that upon re-annealing in air (4), the curve starts to trace the one measured in air during cooling (1) at ~475°C, demonstrating that the conductivity has been recovered to its initial state and that the sample has been re-oxidized.

In Fig. S 3b, Seebeck coefficient measurements are shown. It can be observed that upon re-annealing in air (4), the increased magnitude of Seebeck coefficient at lower temperatures, which appeared during annealing in N_2, is still present. Another observation is that upon re-annealing in air (4), the curve starts to trace that measured during cooling in air (1) already at temperatures below ~300 °C. These results demonstrate that the sample has been returned into its initial state already at this temperature. Finally, it can be observed that the curves (1) and (5) completely coincide over the whole measurement range.

Considering that the ends of the curves (1) and (5) coincide in both measurements, it can be concluded that the changes observed between annealing in air and N_2 are reversible, thus related

to redox processes and not some secondary phenomenon, e.g., formation of secondary phases as it was concluded in the main paper.

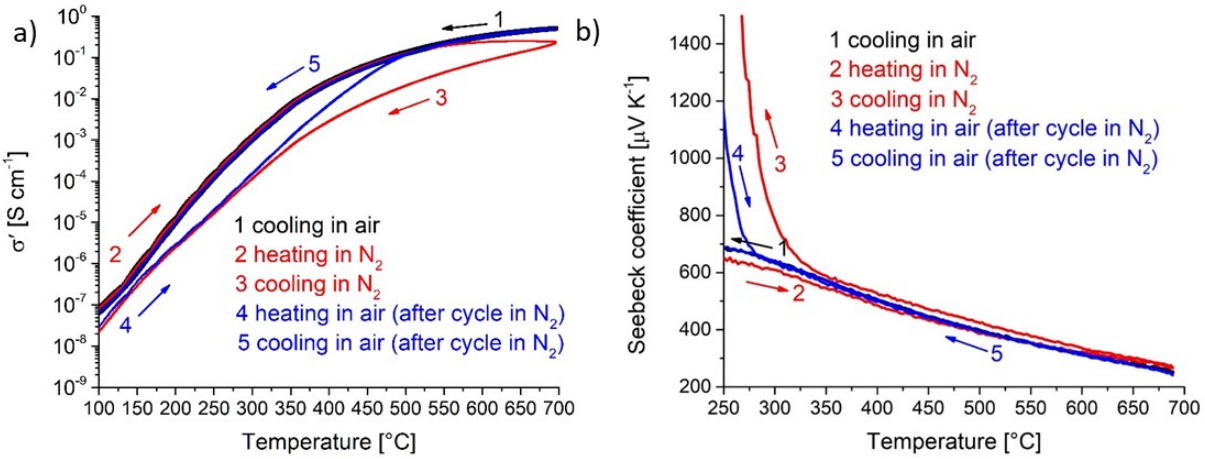

Fig. S 3: a) σ′ and b) Seebeck coefficient as a function of temperature and annealing atmosphere for 1.5 at% Co doped BFO ceramics. Curves 1, 2, 3, 4 and 5 correspond to cooling in air, heating in N_2, cooling in N_2, heating in air and cooling in air, respectively.

Figure S4. Electron paramagnetic resonance (EPR) measurements of 1.5 at% Co doped ceramics

The temperature dependence of EPR spectrum in as-sintered 1.5 at% Co doped BFO is displayed in Fig. S 4a. It can be observed that at temperatures below 300 °C no distinct peaks can be seen, however, the spectra at 200 °C shows two weak peaks (see inset in Fig. S 4a). Another observation is that as the temperature increases from 300 °C to ~360 °C, the center of the spectrum (which corresponds to g -value) is shifting, indicating the contributions of static internal fields due to antiferromagnetic ordering. However, it can be observed that the center of the spectrum is not shifting in the temperature range 370-400 °C, hence, only intrinsic contributions can be observed within this temperature range. This is consistent with the temperature of antiferromagnetic to paramagnetic transition of BFO (T_N = 370 °C) [3].

The EPR spectra of as-sintered, N_2- and 10-atm-O_2-annealed samples (empty symbols) are shown in Fig. S 4b together with the corresponding simulated spectra (full line). It can be clearly observed that these simulation results are in good agreement with experimental data. The values obtained by numerical spectral simulations are presented in Table S 1.

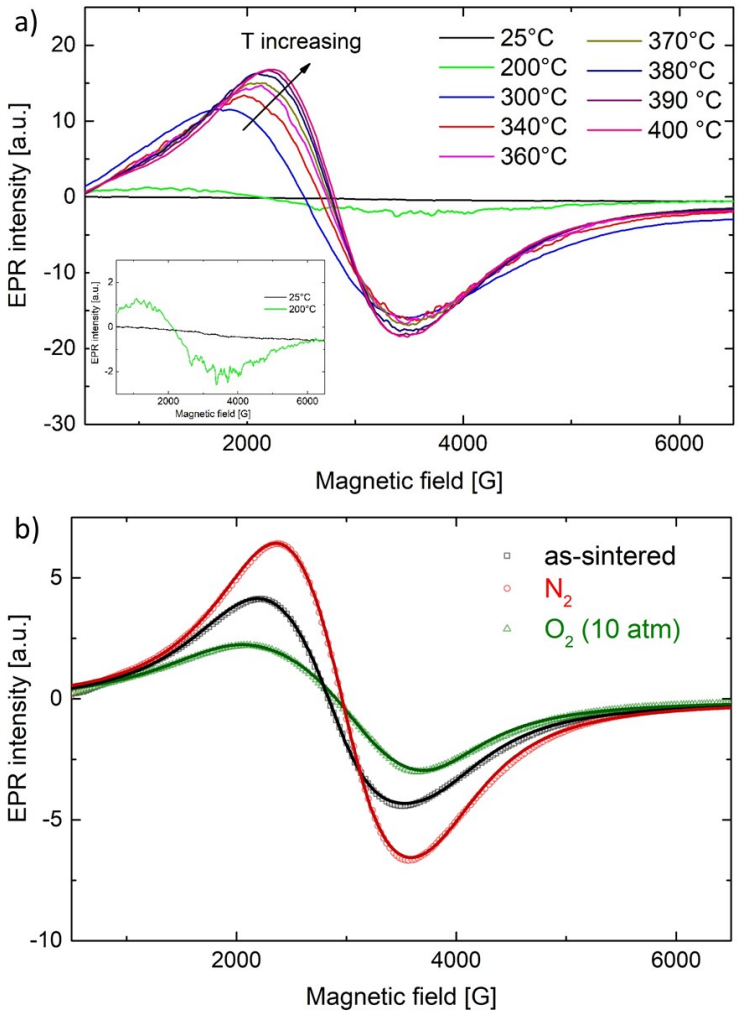

Fig. S 4: EPR measurements of 1.5 at% Co doped BFO ceramics : a) Temperature dependence of the EPR spectum of as-sintered sample. The arrow denotes the direction of increasing temperature. b) EPR spectra of as-sintered, N_2- and 10-atm-O_2-annealed sample (empty symbol) together with numerical spectrum simulations (full line).

Table S1. Numerical simulation of EPR spectra in 1.5 at% Co doped BFO ceramics

Table S 1: The EPR spectral simulation parameters of as-sintered, N_2-annealed and 10-atm-O_2-annealed 1.5 at% Co doped BFO ceramics.

Sample	g factors	Linewidth [mT]	Amplitude (surface)
As-sintered	$g_x = 1.80$	141	895
	$g_y = 3.13$	177	
	$g_z = 2.36$	126	
N_2-annealed	$g_x = 1.82$	140	1186
	$g_y = 2.90$	164	
	$g_z = 2.28$	122	
10-atm-O_2-annealed	$g_x = 2.23$	149	668
	$g_y = 3.38$	209	
	$g_z = 1.84$	132	

Figure S5. The influence of annealing atmosphere on domain switching in 0.25 at% Co doped ceramics

In Fig. S 5 *P-E* hysteresis loops of 0.25 at% Co doped BFO ceramics after annealing in O_2 and N_2 are displayed along with the *P-E* loop of as-sintered sample as a reference. The difference between *P-E* loops of as-sintered and O_2-annealed sample is practically negligible. On the other hand, the polarization response after annealing in N_2 is reduced.

The concentration of the Co dopant (0.25%) in this composition is relatively low, thus it is assumed that also the concentrations of Co'_{Fe} and extrinsic $V_O^{\bullet\bullet}$ and $Fe^{\bullet}_{Fe}$ are low. This means that the defect chemistry in this composition is probably governed by intrinsic defects, i.e., V'''_{Bi}, $V_O^{\bullet\bullet}$ and $Fe^{\bullet}_{Fe}$. The small difference between *P-E* loops of as-sintered and O_2-annealed sample could be explained with comparable concentration of $V_O^{\bullet\bullet}$ in both samples. On the other hand, pronounced pinching (hardening) observed after annealing in N_2 could be explained with promoted formation of $V_O^{\bullet\bullet}$, which act as strong pinning centers.

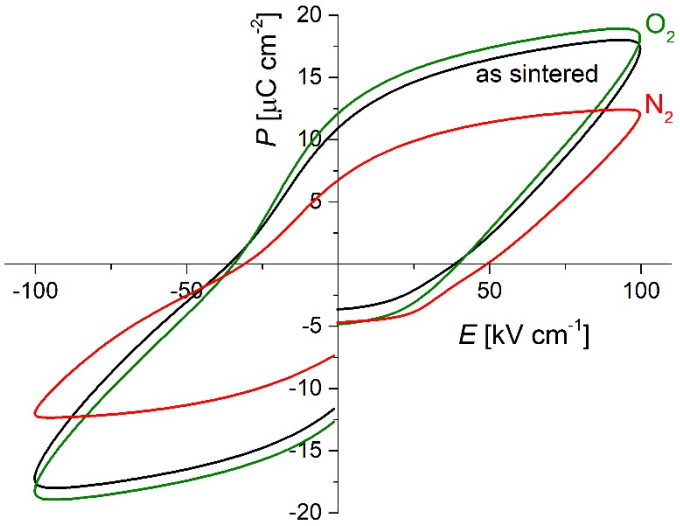

Fig. S 5: P-E loops of as-sintered 0.25 at% Co doped BFO ceramics, annealed in 10 atm O_2 and N_2 at 100 kV cm^{-1}.

Figure S6. *In-situ* measurements of Seebeck coefficient and AC conductivity as a function of temperature and annealing atmosphere in 0.25 at% Co doped BFO ceramics

In Fig. S 6a, the real part of the AC conductivity (1 Hz) is shown. The conductivity increases with increasing temperature, as expected. It can be seen that upon heating in N_2 (2), the curve traces that measured in air during cooling (1) only up to ~550 °C when the conductivity reaches plateau and deviates from the trend measured in air (compare curves 1 and 2 above 550 °C).

Upon cooling in N_2 (curve 3), the conductivity decreases as expected, however, the absolute conductivity value is lower than that measured during heating in N_2 (2). The decrease of conductivity during annealing in N_2 is in line with p-type behavior. In the real part of dielectric permittivity presented in Fig. S 6d, a strong step-like feature appears during cooling in N_2 (3), accompanied by a peak in $\tan\delta$ (indicated by green arrow), which has been tentatively attributed to a Maxwell-Wagner (M-W) relaxation (see paper, Figure 5 and text for explanation).

The Seebeck coefficients of 0.25 at% Co doped BFO ceramics (see Fig. S 6d) are positive in air and N_2, confirming p-type conductivity and indicating that Fe^{4+} are major charge carriers. However, upon cooling in N_2, the magnitude of Seebeck coefficient increases at lower temperatures, which is probably related to inhomogeneous reduction in N_2 (see paper, Figure 5 and text for explanation).

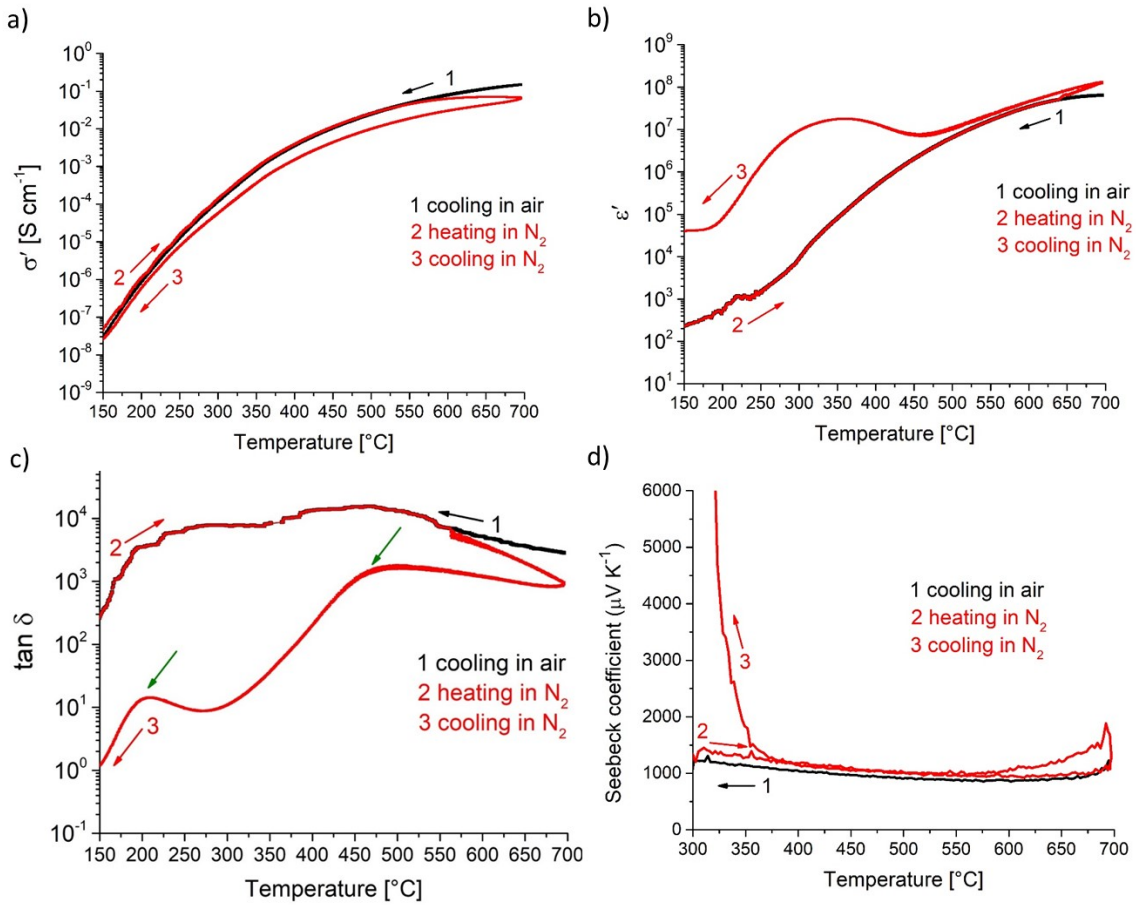

Fig. S 6: a) The real part of the AC conductivity (1 Hz), b) real permittivity, c) $\tan\delta$ and d) Seebeck coefficient as a function of temperature and annealing atmosphere, i.e., synthetic air and N_2, for 0.25 at% Co doped BFO ceramics. Curves 1, 2 and 3 correspond to cooling in air, heating in N_2 and cooling in N_2, respectively. Green arrows indicate peak in $\tan\delta$.

References

[S1] S.H. Skjærvø, E.T. Wefring, S.K. Nesdal, N.H. Gaukås, G.H. Olsen, J. Glaum, T. Tybell, S.M. Selbach, Interstitial oxygen as a source of p-type conductivity in hexagonal manganites, Nat. Commun. 7 (2016). doi:10.1038/ncomms13745.

[S2] T. Rojac, A. Bencan, G. Drazic, N. Sakamoto, H. Ursic, B. Jancar, G. Tavcar, M. Makarovic, J. Walker, B. Malic, D. Damjanovic, Domain-wall conduction in ferroelectric BiFeO 3 controlled by accumulation of charged defects, Nat. Mater. 16 (2017). doi:10.1038/nmat4799.

[S3] G. Catalan, J.F. Scott, Physics and Applications of Bismuth Ferrite, Adv. Mater. 21 (2009) 2463–2485. doi:10.1002/adma.200802849.